Contents lists available at ScienceDirect

Colloids and Surfaces A: Physicochemical and Engineering Aspects

journal homepage: www.elsevier.com/locate/colsurfa

Sequential droplet reactions for surface-bound gold nanocrater array

Tulsi Satyavir Dabodiya [a,b], Haitao Yu [c], Miaosi Li [c,*], Xuehua Zhang [a,d,**]

[a] *Department of Chemical and Materials Engineering, University of Alberta, Alberta T6G 1H9, Canada*
[b] *Centre for Nanoscience and Technology, Madanjeet School of Green Energy Technologies, Pondicherry University (A Central University), Dr. R. Vankataraman Nagar, Kalapet, Puducherry 605014, India*
[c] *School of Engineering, RMIT University, Melbourne, Victoria 3001, Australia*
[d] *Physics of Fluids Group, Max Planck Center Twente for Complex Fluid Dynamics, JM Burgers Center for Fluid Dynamics, Mesa+, Department of Science and Technology, University of Twente, Enschede 7522NB, the Netherlands*

GRAPHICAL ABSTRACT

Arrays of catalytic gold nanocraters (GNCs) are formed and bounded on a surface from reactive femtoliter droplets. The catalytic activity of GNCs were evaluated by degradation of both anionic and cationic azo dyes in water. This strategy represents a solution-based approach for the formation of surface-bound catalytic nanostructures based on sequential droplet reactions.
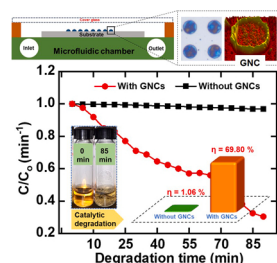
ARTICLE INFO

ABSTRACT

Femtoliter droplet array exhibit unique stability in contact with a flow. This work demonstrates that reactive femtoliter droplets enables sequential chemical reactions that may be leveraged to simplify the process for producing surface-bound materials. Gold nanocraters (GNCs) are formed on a planar substrate from biphasic reactions between water-insoluble thiol droplets and two aqueous solutions in sequence. The detailed process is that gold precursor solution was injected into a flow chamber hosting a substrate with thiol droplet array in a chamber, followed by injection of a reductant solution. The thiol droplets absorb and weakly bond with gold ions in a precursor solution. Subsequent exposure to a reductant solution accelerates the formation of gold clusters in droplets. The final nanoparticles form GNCs over a large surface area, due to fast formation around the droplet rim. The shape of an individual domain was controlled by the duration of ion absorption in the first step of the sequential reaction. Reacting droplets were followed in time by total internal reflection microscope to understand the reaction process. Morphology and composition of GNCs were characterized by atomic force microscope, SEM, microspectrophotometer, and X-Ray photoelectron spectrometer. We demonstrate that the as-prepared GNCs exhibits stable catalytic activity in degradation of azo dyes for multiple cycles. Compared to many current approaches for producing surface-bound nanomaterials, our approach is based on sequential droplet reactions in a flow-in process. This approach offers unique flexibility in varying independently the

* Corresponding author.
** Corresponding author at: Department of Chemical and Materials Engineering, University of Alberta, Alberta T6G 1H9, Canada.
  E-mail addresses: miaosi.li@rmit.edu.au (M. Li), xuehua.zhang@ualberta.ca (X. Zhang).

reactant concentration and reaction time of each step in the sequential reaction. The synthesized surface-bound catalytic nanomaterials may be applied in water treatment, optical display or fluorescence imaging.

1. Introduction

Extremely small droplets are of paramount significance in many advanced technologies including water collection from foggy atmosphere, artificial rainfall in arid areas, and sample preparation in biomedical diagnostics and chemical analysis [1]. Droplets provide a confined environment in synthetic chemistry to realize cascade reactions in a fashion similar to artificial cells. The surface of microdroplets serves as a biphasic site for catalysts to access immiscible liquid phases inside and outside of droplets, significantly improving specificity and efficiency of interfacial catalytic reactions [2,3]. Regarded as a green and sustainable approach, droplet reactions provide clear advantages for chemical reactions, due to the spatial separation of reagents or products between the droplets and the surrounding. Small droplets may enable efficient chemical conversion under mild conditions [4], particularly suitable for biphasic reactions between two immersible phases [5–8,9]. Beyond significant acceleration in reaction rate, compartmentalization of the droplets may even trigger spontaneous reactions that would be thermodynamically unfavorable in bulk [10, 11]. Despite the significance for a broad range of technological applications, it remains challenging to predict and control sequential reactions of microscopic droplets for desired products.

Surface-bound nanomaterials are required for various applications such as clean water collection, photocatalytic electrolysis in energy conversion, tactile sensors and artificial skin. Many surface-bound nanomaterials rely on the surface arrangement to maximize performance, for example, for the signal detection in sensors, surface enhanced Raman spectroscopy [12,13], light-substrate interactions in solar energy harvesting [2,14–16], or heat and mass transfer in catatlytic conversion [17–19]. Chemical reaction with surface droplets may potentially streamline the process of synthesis and immobilization of surface-bound nanomaterials to obtain desired spatial arrangement and surface coverage of nanostructures. Distinct from common techniques for depositing nanomaterials on the substrates such as direct growth [20], dip coating, sputter [21], chemical or physical binding [22–24], droplet reactions may take place on substrates with arbitary shape and size during both formation of reactive droplets and production of nanomaterials.

Solvent exchange is a newly established simple process for formation of femtoliter surface droplets [25,26]. Here femtoliter surface droplets refer to liquid droplets on a solid surface in contact with a surrounding liquid that is immersible. [25,27] The height of femtoliter droplets ranges from tens to few hundreds nanometers. Their base diameter is 0.1–100 μm, determined by wettability and hydrophobic or hydrophilic micropatterns on the substrate surface. The size, location and composition of the droplets are fine tuned by solution composition and level and duration of the oversaturation during the solvent exchange. [25,26, 28] Femtoliter droplets can form substrates of varied shape or size from a planar wafer to the inner or outer walls of a microcapillary tube. [26] Location and surface coverage of femtoliter droplets are controlled by chemical wetting patterns on the surface. [26].

Synthesis of nanomaterials from droplet reactions requires understanding and control of the reaction rate. For a biphasic reaction between droplets and the surrounding, the overall rate is determined by both intrinsic kinetics of the reaction and mass transfer cross the droplet surface [29,30]. Compared to spray droplets flying in air [31,32], the three-phase contact lines of these femtoliter droplets are pinned by the solid surface [33], providing much needed stability of droplets to an external flow. Hence both the concentration and the sequence of the reactants in the surrounding can be controlled by the flow of reactant solutions. Although on-droplet reactions have been reported for

extraction and sensitive chemical analysis, [29] and for one-step synthesis of the precursor structures [1,34,35], the potential for sequential reactions of stable femtoliter droplets remains to be explored for synthesis of a wide range of surface-bound catatlytic nanomaterials.

In this work, we demonstrate sequential droplet reactions for controlled formation of gold nanocraters. In the first step, thiol droplets acted as host platform for gold ions with precise location over the patterned substrate within the flow chamber. In the second step, the flow of a reductant solution further assisted the formation of gold hosted droplets into the final gold nanocraters (GNCs). The substrate with surface-bound GNCs was then used for catalytic activity in the degradation of both anionic and cationic azo dye degradation in water. Our work demonstrates sequential droplet reactions as a novel route for insitu synthesis of surface-bound catalytic metal nanostructures in an ordered array over a large surface area.

2. Experimental section

2.1. Materials

Ethanol (90%), octadecyltrichlorosilane (OTS, 98.9%), sodium citrate dihydrate (99%), rhodamine B (RhB) (99%), methyl orange (MO) (99%) and methylene blue (MLB) (93%) were all purchased from Fisher Chemical (Canada). Gold (III) chloride trihydrate (100%) and 1-dodecanthiol (DT, 98%) were purchased from Sigma Aldrich (Canada). Water was obtained from a Milli-Q purification unit (Millipore Corporation, Boston, MA). Cover glass (Fisher Scientific) and silicon wafer (University wafer, USA) were used as substrates. The hydrophobic microdomains on hydrophilic substrates were fabricated by photolithography following an already reported protocol [34]. The scale of the obtained hydrophobic microdomains was 5 ± 0.1 μm in diameter with 7.5 ± 0.1 μm center-to-center distance.

2.2. Formation of gold nanocraters (GNCs) by solvent exchange process

The reactive nanodroplets were produced on the microdomians by solvent exchange process. In the process, a prepatterned substrate was placed in a flow chamber (Figure S1) measuring 0.63 mm in height, 15 mm in width, and 150 mm in length. DT dissolved in ethanol at the concentration of 2% v/v (solution A) was introduced into the flow chamber first, followed by water (solution B) at the flow rate of 100 $\mu L/$min. This process generated DT droplets on the pattern of hydrophobic microdomains. Following that, a 3 mg/ml $HAuCl_4$ aqueous solution was pumped into the system at the same flow rate for an appropriated time. Afterwards gold ions absorbed on the droplet surface. Appropriate volume of water was flowed in at the rate of 100 μL for 10 min to remove excess gold precursors from the chamber and do wash of physically absorbed precursors from hydrophilic area of the patterned substrate. Subsequently, a sodium citrate aqueous solution was exchanged at a rate of 100 μL to reduce the gold-thiol complex droplets into GNCs.

2.3. Characterization of nanodroplets and GNCs

DT surface nanodroplets were imaged by an upright optical microscope (NIKON H600l or Huvitz HRM-300) coupled with a 10 × or 100 × lens. The formation process of GNCs from reactive droplets was monitored by total internal reflection fluorescence microscopy (TIRF, 100 × objective lens, Nikon). The morphology of surface of the GNCs was characterized by atomic force microscopy (AFM, Dimension Icon-Bruker). Field Emission Scanning Electron Microscope (FESEM) was performed on a FEI Nova NanoSEM 200 at 5 kV and a working distance

Table 1
The conditions of catalytic reaction. The volume is 2 ml for all three tests.

Dye	Concentration (mM)	$NaBH_4$
MO	1	0.5 ml
MLB	0.1	0.2 ml
RhB	5	0.2 ml

of 4.7 mm to characterize the morphology. The surface chemistry of GNCs was characterized using a K-alpha X-Ray photoelectron spectrometer (XPS, Thermo Scientific). The incident radiation was provided by a monochromatic Al Kα X-rays (1486 eV) at 72 W (6 mA and 12 kV). A low energy flood gun was used to compensate the surface charging effect. All data were processed using CasaXPS software, and the energy calibration was referenced to the C 1 s peak at 284.8 eV. The absorption spectra of GNCs were measured using a microspectrophotometer (20/30 PVTM, CRAIC Technologies Inc.).

2.4. Evaluation of catalytic activity

All of the catalytic measurements were performed under ambient conditions. A (0.8 cm × 1.5) cm with dimension of patterned GNCs substrate was used for evaluation of catalytic activity of GNCs. A 2.0 ml aqueous solution of anionic or cationic model dyes used for catalytic reaction concentrations and GNCs substrate are listed in Table 1. 0.06 M of $NaBH_4$ was used during catalytic activity. After certain interval, 0.5 ml of the dye solution was collected and placed into plastic UV-transparent disposable cuvettes. For UV measurement, the sample was added again into the base solution moderately. UV-Vis spectroscopy (GENESYS 150) was used to obtain the absorbance spectra of different dyes during GNC catalyzed degradation activity. During the reusability test, the same GNCs substrate was used in three consecutive cycles for MO degradation. The extent of dye degradation was calculated using equation 1 given below.

$$Degradation\ efficiency(\%) = \frac{A_o - A_t}{A_o} \times 100\% \tag{1}$$

Here, A_o is the initial absorbance of the dye solution and A_t is the absorbance at different time of the dye degradation.

3. Results and discussion

3.1. Droplet localized formation of GNCs

After, the ordered array of DT droplets were produced on hydrophobic microdomains by solvent exchange. The sequence of the different solutions introduced is shown in Fig. 1A. Due to the insoluble nature of DT in water, the droplets in the array remain stable when water is displaced by a flow of an aqueous solution of Au(III) precursors (solution C), as shown in Fig. 1B. Through Au-S bonds, the thiol (-SH) group of the DT droplet interacts with gold ions in the solution to form an intermediate Au-thiol complex. Subsequent exposure of the reactive droplets to a solution of sodium citrate, a strong reducing agent (solution D), completes the reduction of Au(III) to GNCs, as the darker droplet
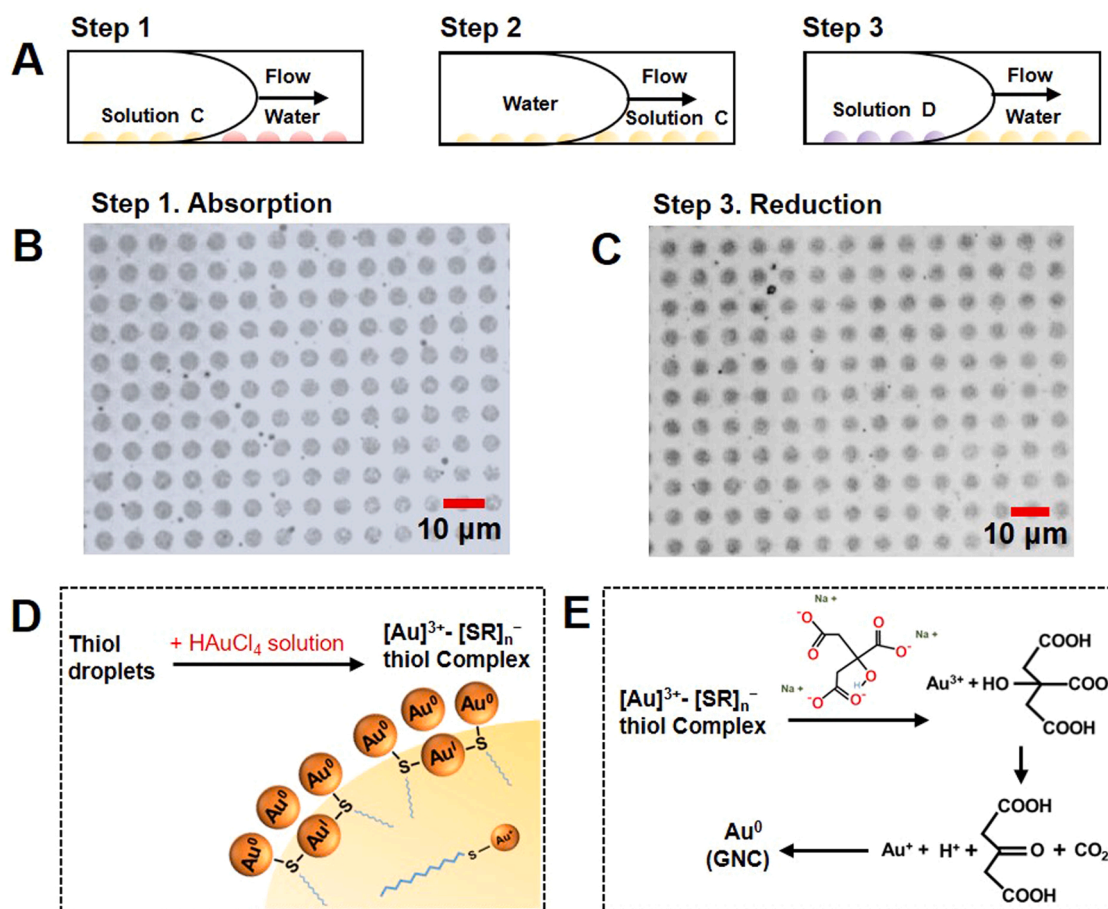

Fig. 1. The formation process of GNCs. (A) $HAuCl_4$ precursor solution (Solution C) is injected into the chamber (step 1), Water is injected to remove extra $HAuCl_4$ precursor residues (step 2). At last, Sodium citrate precursor (Solution D) injected (step 3). (B) Optical image of gold ions absorbed over thiol droplets during step 2. (C) Optical image of gold ions reduced to gold during step 3. (D) Mechanism of thiol-gold complex formation via absorbance, and (E) gold reduction form Au(III) to Au(0).
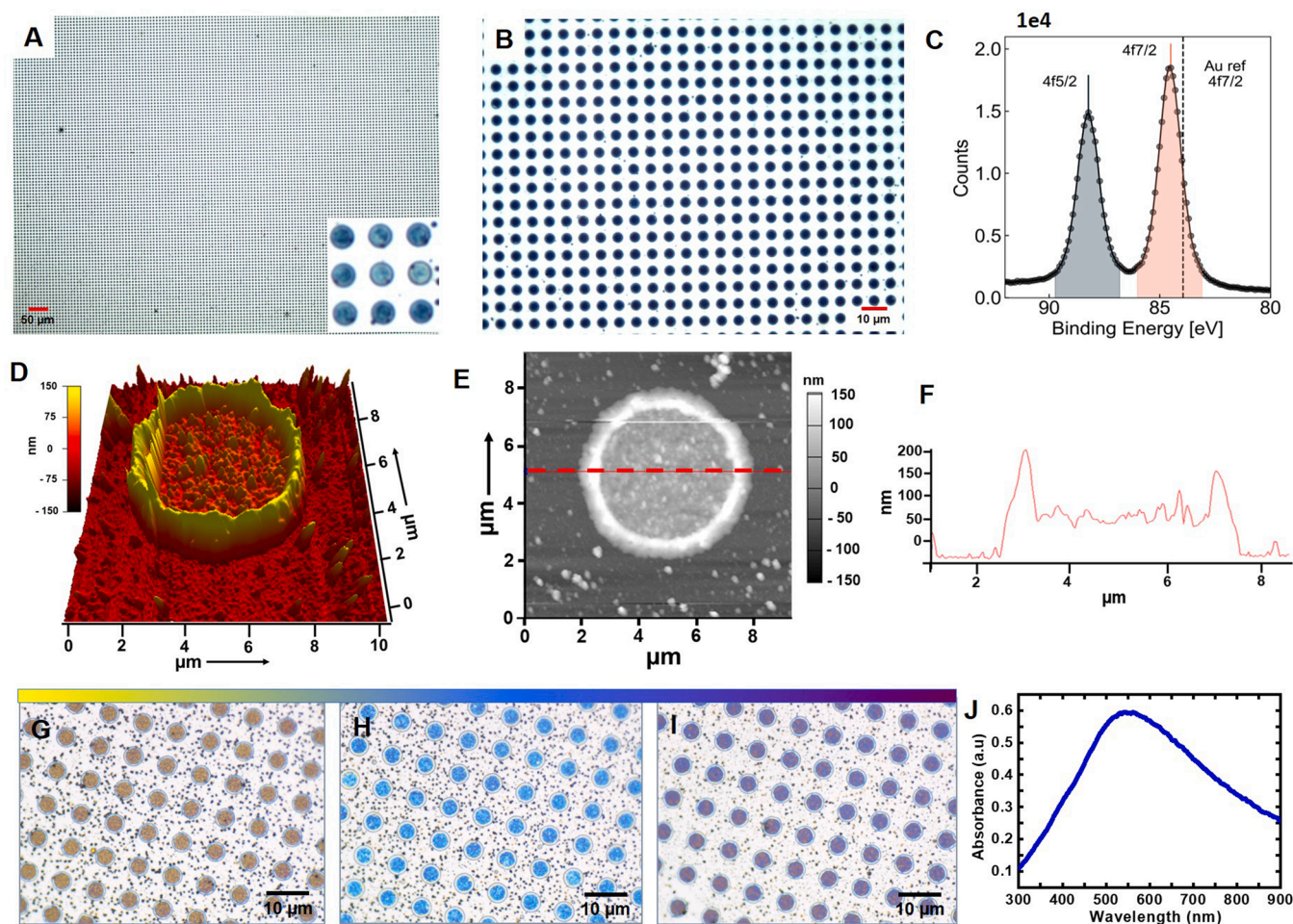
Fig. 2. Morphology and properties of GNCs. (A,B) Optical images of highly ordered array of GNCs in air with a zoomed image as insert in (A). (C) XPS spectra of GNCs. The reference for Au 4f7/2 is indicated by the dashed line at 83.95 eV. (D) 3D view and (E) top view of GNC in an AFM image. (F) Cross-sectional profile of a GNC as marked by the dotted line in (E). (F) Cross-sectional profile of a GNC as marked by the dotted line in (E). (G-I) Different colors observed from GNCs located along the flow direction. (J) UV-Vis absorbance spectrum of a representative GNC.

patterns are observed in Fig. 1c. When the solution is removed, the GNC patterns remain immobilised on the substrate.

The detailed mechanism of GNC formation is proposed in Fig. 1D and E. When the $HAuCl_4$ precursor solution was in the contact with DT droplets, the Au (III)-S binding takes place to confine the diffused Au(III) ions onto the DT droplet surface, by forming an intermediate $[Au-SR]_n$ complex (Fig. 1D) [36]. Although the Au(III)-S bond is weaker than the Au (0)-S bond, the extremely large surface area of the droplets would enhance the interaction efficiency [] ensuring sufficient Au(III) incorporation with the droplets. Due to the reductive ability of thiol, a portion of the Au(III) in the intermediate product can also be reduced to Au(I). The formation of Au(I) contributes to the reduction of Au(III) to Au(0) by lowering the energy and increasing the ligand exchange rates.[37] When the excess Au(III) precursor in bulk is removed by flushing water prior to the addition of the reducing reagent, sodium citrate, Au(III) ions are confined to the surface of DT droplets and are ready for the localized reaction. Upon addition of the citrate agent, the intermediate Au-thiol complex is completely reduced from Au(III) $\Leftarrow$ Au(I) and Au(I) $\Leftarrow$ Au (0) (Fig. 1E). Following that, the nucleation and aggregation occurs, allowing for the final structures. The GNCs remains stable when the substrate is taken out from the chamber and the medium phase transferred from liquid to air.

3.2. Morphology of the GNCs

The array of GNCs in air exhibits vivid color (Fig. 2 A, B). The consistent color presented over the large substrate surface demonstrated the uniform interaction between droplet and bulk medium, benefiting from the laminar flow in the narrow channel. The characteristic spacing of 4f7/2 and 4f5/2 orbitals in the high-resolution XPS reveals the presence of Au in Cs (Fig. 2 C). The peak of the sample exhibits a distinct shift of $\sim$ 0.61 eV to $\sim$ 84.56 eV. Additionally, the full width at half maximum (FWHM) is $\sim$ 1.1 eV, higher than 0.76 eV expected from the Au reference. Both the shift and broadening of the peaks are associated with the presence of gold-thiolate nanoclusters rather than individual gold atom [38]. These results are consistent with those obtained by Negeshi et al. for 1.8 nm gold nanoclusters [39]. These species are expected to provide high thiol to Au precursor ratio in the droplet reaction in confined duration.

A clear 3D view of a GNC formed in an individual droplet captured by AFM in Fig. 2D-f unveils that the lateral size of the nanocrater was 5 μm with a concentric ridge around the periphery. The line profile laterally across the nanocrater measures the maximal height of concentric ridge of $\sim$ 200 nm. The surface of the trough part inside the GNC is rough with height of 50–100 nm above the flat surrounding area. The morphological analysis of GNC is further characterized by using FESEM images shown in Figure S1. The size, distinct arrangement as well as regular distribution of final developed GNCs on substrate in FESEM images
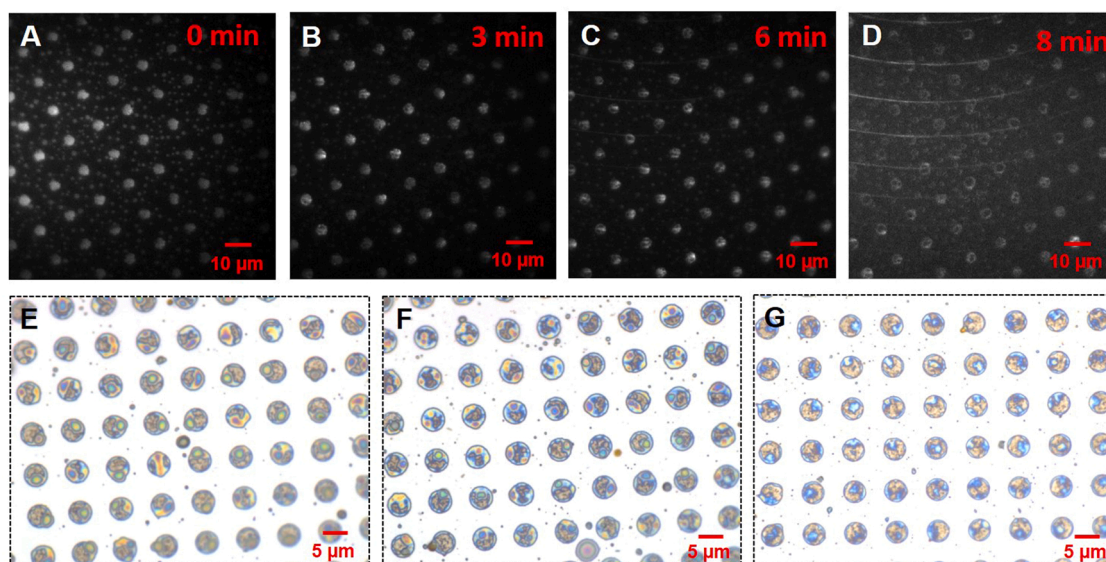
Fig. 3. TIRF images of final GNCs at different duration of gold precursor exchange using nile red as a fluorescent agent. (A) Droplet with no gold precursor exchange. (B) For 2 min of gold precursor exchange. (C) For 5 min of gold precursor exchange. (D) For 8 min of gold precursor exchange. Effect from the initial thiol concentrations when gold precursor exchange constant duration over the final morphology of gold nanocraters. Optical image of incomplete GNC pattern in absence of reduction. (E) After 30 min adsorption of Au^{3+} with thiol. (F) and (G) Left for 1 hr and 24 hrs in air.

evidently concede with aforementioned AFM studies.

Plasmonic effect of gold nanoparticles results in the various optical properties of GNC when formed with different nanostructures. For example, images in Fig. 2G-I captured the different colors of GNCs under the bright field of microscope. These GNCs were fabricated inside a chamber with varied local droplet conditions along the flow direction. The UV-Vis spectrum in Fig. 2J shows a wide absorbance band of a representative GNC ranging from 450 to 700 nm with a peak center at ∼ 550 nm. The absorbance peak demonstrates the existence of Au nanoparticles in GNCs and the broad absorption bandwidth reveals a relatively broad size distribution of Au NPs, which may bring an enhanced sensitivity of the GNCs to light in future photonic applications based on localized surface plasmon resonance, similar to a thin film with attached Au nanoparticles [40].

3.3. Au ion absorption at DT droplet surface

Thiol-gold clusters in the droplets may quench the fluorescence intensity of a dye, a property that was used to follow the changes of droplets after the absorption of Au ions. Droplets doped with fluorescent dye, nile red, were followed at the excitation wavelength of 561 nm using TIRF microscopy as shown in Fig. 3 (A-D). Immediately after contact with auroic solution in step 1, all the droplets were evidently observed by the evanescent wave from total internal reflection near to the substrate to the strong fluorescent intensity of droplets. After gold precursor was injected into the chamber for different times (3, 6, and 8 min), the fluorescent intensity of the droplets gradually became weaker. The fluorescence signal almost disappeared from the middle of the droplet and faded around the droplet after 8-min. The above changes in fluorescence quenching of the droplets might signify the development
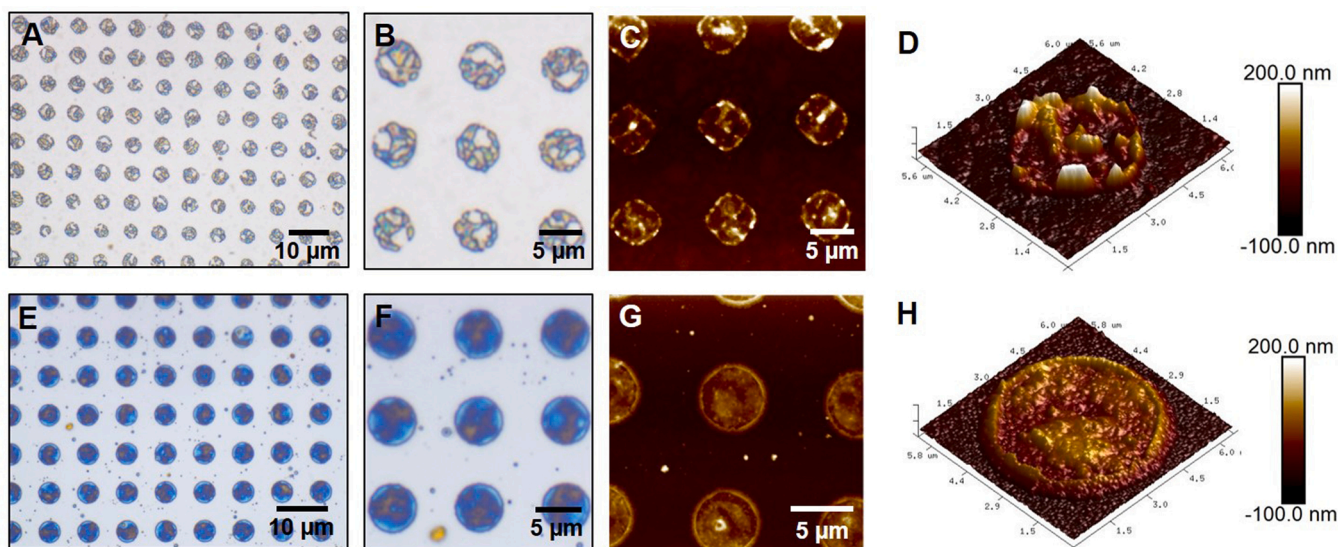

Fig. 4. Effect of duration for absorption of auric ions. (A) Optical image of GNCs from 2-min absorption (underdeveloped GNCs). (B) Magnified optical image of (A). (C) AFM image of 2 min absorption. (D) Profile of underdeveloped gold nanocrater by 2 min exchange. Optical images of, (E) Absorption for 5 min (morphology of developed GNC). (F) Magnified optical image of (E). (G) AFM image of 5 min exchange of gold precursor solution. (H) Profile of developed GNC by 5-min absorption.
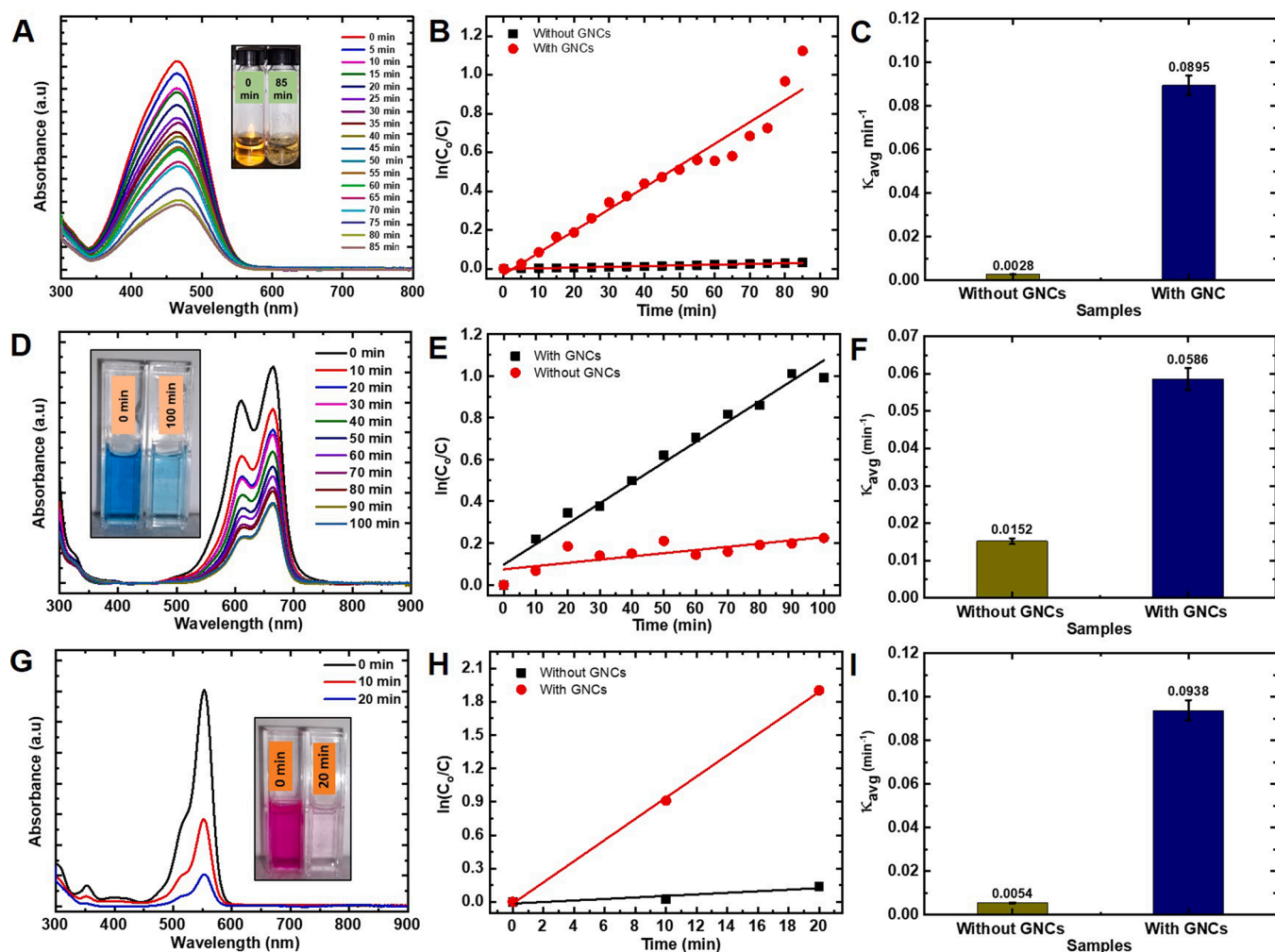
Fig. 5. (A) UV absorbance spectra of MO aqueous solution using GNC substrate. (B) Kinetics of degradation of MO in the aqueous solution. (C) Average rate kinetics of degradation of MO during the degradation process. (D) UV absorbance spectra of MLB aqueous solution using gold nanocraters substrate. (E) Kinetics of degradation studies of MLB aqueous solution. (F) Average rate kinetics of degradation of MLB during the degradation process.(G) UV absorbance spectra of RhB aqueous solution using gold nanocraters substrate. (H) Kinetics of degradation studies of RhB aqueous solution. (I) Average rate kinetics of degradation of RhB during the degradation process.

of GNCs into a peripheral ring during Au ion absorption. The absorption of Au ions was terminated at 30 min by taking the substrate out of the flow chamber without reduction. The color of GNCs in optical image (Fig. 3E) was pretty uneven. After these substrates were exposed in atmosphere for 1 h and 24 h, no obvious difference was found in the droplet color in Fig. 3 F,G, suggesting no further reaction took place in air and thus the reduction with citrate could contribute to the formation of a more uniform GNC array.

In addition, the final morphology of GNCs also depended on the duration of auric ion absorption. Au absorption took nearly 2 min which was then reduced by citrate, the final morphologies of these underdeveloped GNCs were characterized by optical microscopy and AFM, and shown in Fig. 4 A-D. For an individual GNC, the rim was not fully integrated to be a concentric ridge and the trough at the middle of GNCs was rough with obvious bumps. As the duration of Au ion absorption was extended to 5 min, GNCs developed into the morphology of typical concentric ridge around the periphery as given in Fig. 4 E-H. The differences between the final morphologies of GNCs in two cases could be attributed to number of nuclei formed over the droplet in step 1[41]. During absorption of Au ions, the large specific surface area of ordered thiol droplets provide active sites for absorption Au ions. the ions may also diffuse into the droplet. With a shorter absorption time (i.e. 2 min), the amount of retained gold ions could not be sufficient so that the

converted product could not cover the whole base area of the droplet. Sporadical nucleation of the gold complex led to development of an irregular shape after reduction by citrate. As the absorption time extended to 5 min, larger amount of Au ions bind with thiol droplets and more product were formed to cover the droplet surface.

It is interesting what leads to the final shape of GNCs. In previous work, silver nanoparticles were synthesized from droplet reaction with silver precursor solution.[42] The final structure consisted of clusters of silver nanoparticles on the droplet base area. In contrast, from droplet reaction, porous metal oxides took the shape of nanocaps with spatial arrangement and surface coverage predetermined by droplets, [43] resembling a superparticle assembly from evaporation of multicomponent droplets [44]. In the case of polymeric microdents with a crater shape, droplet liquid dissolved the superficial polymer layer, and then the dissolved polymer was deposited preferentially along the rim during droplet dissolution[45]. There was no chemical reaction involved, apart from swelling, dissolution, and deposition of the polymer. Different preferential deposition, faster formation of the product around the rim than on other area of the droplet surface may also lead to more deposit on the edge. Faster reduction of gold-thiol complex may explain the shape of gold craters observed in this work. This mechanism is consistent with our latest work, where faster reaction rate along the rim was attributed to the faster microbubble formation from the gas product in
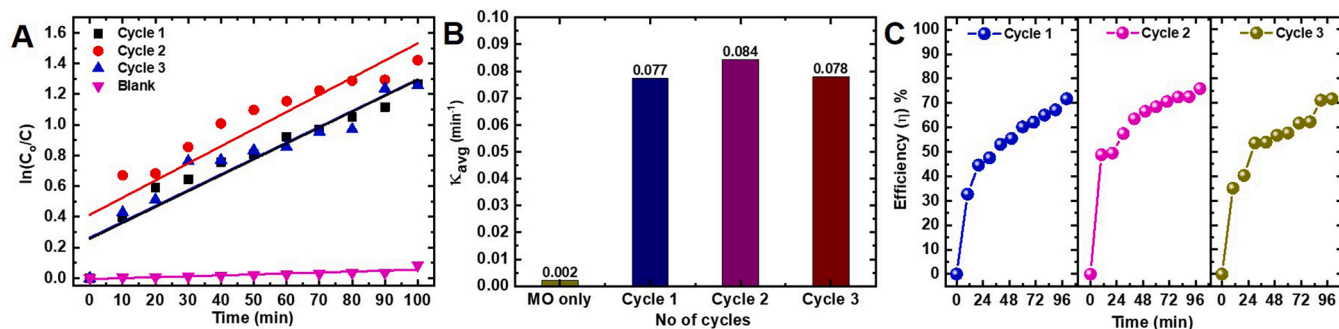
Fig. 6. Degradation behaviors for 3 consecutive cycles during recyclability test, (A) Kinetics of degradation studies of MB aqueous solution during three cycles, (B) Average rate kinetics of degradation of MO during 3 cycles in degradation process, (C) Degradation efficiency during each cycle.

the droplet reaction [46,47].

3.3.1. GNCs catalyzed dye degradation

Catalytic activity of GNCs was first determined by reducing an anionic dye, MO on a GNC substrate in the presence of $NaBH_4$ in the dye solution. The characteristic absorption peak of MO was located at 465 nm in a UV–vis spectrum in Fig. 5A. The intensity of the peak gradually decreases in the presence of a GNC substrate immersed in the solution. The disruption of the chromophoric structure in MO is catalyzed by GNCs. After 85 min, the degradation of MO in the solution reached 70%, indicating that the majority of MO in the solution had been degraded. In comparison, the absorbance of MO solution in the absence of GNC substrate does not significantly decrease after 85 min of interaction with $NaBH_4$, as shown in Figure S2a.

The catalytic degradation rates (C/C_0) of MO are plotted in Fig. 6. Additionally, the Langmuir-Hinshelwood model was used to quantify the reaction kinetics of MO degradation in the presence and absence of GNC substrate.[48–50] The kinetic rate constants were determined as follows using the first-order kinetic equation 2:

$$\frac{dC_t}{dt} = \frac{dA_t}{dt} = -K_a t \tag{2}$$

where, C_t is concentration of MO at time t.

The concentration of MO can be determined by its absorbance intensity (A_t) at 465 nm. After integrating equation 2 with the absorbance, we can obtain Eq. (3) to quantify the degradation. Where, A_0 and A_t are the initial and final absorbance intensity of MO at 465 nm. C_0 represents the initial concentration of MO at t = 0.

$$\ln \frac{C_t}{C_0} = \ln \frac{A_t}{A_0} = -K_a A_t \tag{3}$$

The catalytic degradation of MO followed a linear pattern and exhibited pseudo first-order kinetic characteristics. The slope of the linear fitted curve in Fig. 5 B yields the kinetic reaction rate constant (K_a). The K_a for GNCs- and non GNCs-facilitated catalytic reaction were determined to be $1.123 \times 10^{-2} min^{-1}$ and $3.796 \times 10^{-4} min^{-1}$, which are comparable to the previous surface based catalyst studies respectively [50–52]. The high reaction rate is attributed to the catalytic capability of GNCs. As shown in Fig. 5 B, the average kinetics values (K_{avg}) for the GNCs catalytic degradation is 0.08951, and 0.00283 min^{-1} without GNC, as shown in Fig. 5 C.

Besides anionic dye, cationic dyes such as methylene blue (MLB) and rhodamine B (RhB) were also used to evaluate the catalytic activity of GNCs. The degradation process of MLB and RhB in the presence of $NaBH_4$ and GNC substrate is shown in Fig. 5 D and G, respectively. The degradation of MLB reaches to 60% with in 100 min of reaction, while 80% of the RhB was degraded after a 20 min reaction. In the absence of GNCs substrate, there was no significant degradation for both MLB and RhB, as shown in Figure S2 in Supplementary Materials.

The rate constant of GNC assisted MLB degradation reaction was

Table 2
The reaction rate for MO dye catalytic degradation cycles.

Reaction	Reaction rate constant (K_a)	Values
Cycle 1	K_{C1}	$1.036 \times 10^{-2} min^{-1}$
Cycle 2	K_{C2}	$1.118 \times 10^{-2} min^{-1}$
Cycle 3	K_{C3}	$1.032 \times 10^{-2} min^{-1}$
MO only	K_B	$0.06 \times 10^{-2} min^{-1}$

found to be 0.978×10^{-2}, nearly 6.4 fold of blank dye degradation rate ($K_a = 0.151 \times 10^{-2} min^{-1}$) with out using GNCs (Fig. 5E). The catalytic degradation rate profiles (C/C_0) of MLB and RhB in presence and absence of GNCs substrate are plotted in Figure in S3. Correspondingly, the average rate kinetics of MLB using GNCs were found higher to be 0.0588 min^{-1} much higher than its counterpart without GNCs (0.01518 min^{-1}) during the degradation process, which is represented in Fig. 5F. Similarly, in the case of RhB, the reaction rate constants are obtained as 9.516×10^{-2} and $0.692 \times 10^{-3} min^{-1}$ with and without using GNCs (Fig. 5H). The average reaction rate constant for the GNCs favored catalytic degradation of RhB was 0.09376 min^{-1}, roughly eighteen times higher than the average rate constant of blank dye degradation ($K_{avg} = 0.00539 min^{-1}$) with out GNCs substrate as shown by Fig. 5I.

The catalytic efficiency of our GNCs appears to be lower than that of other studies ranging from 1.3 to 26 min^{-1}. However, in our tests only a small piece of GNC-coated substrate was immersed in the solution, so the total mass of GNCs contributed to the reaction was small, in comparison to the degradation with catalyst directly added into the solution [53]. The outstanding efficiency from interconnected gold on a filter paper [54,55] or gold nanoparticles in electrospun nanofiber membranes [56] provide important hints for future work. A porous substrate (such as paper or fiberous memberanes) may be used for GNC formation to improve catalytic efficiency.

3.3.2. Reusability of surface-bound GNCs catalytic degradation

The advantage of surface-bounded catalysts is their ease of separation from the reaction medium and their ability to perform repeatable catalytic activity. To determine the reproducibility of GNCs substrates in repeated catalytic reactions, we performed three sets of MO degradation using the same GNCs substrate. Figure S3 clearly depicts the absorbance spectra of catalytic degradation process during cycle 1–3. The corresponding degradation rate constants of cyclic degradation studies included with blank dye degradation without GNCs were deduced by graphs in Fig. 6 A and listed in Table 2. The K_{avg} for the three repeated cycles (0.077, 0.084 and 0.078 min^{-1}) assisted by GNCs potently demonstrate the excellent consistency of GNCs catalytic activity (Inset in Fig. 6 A). The degradation efficiency of each cycle was plotted against reaction time in Fig. 6 C, which suggests that the degradation percentages of MO for cycle 1, 2 and 3 are 71.4%, 75.6% and 71.6%, respectively. The slight discrepancy in the degradation kinetics and degradation efficiency could be associated with the incomplete removal
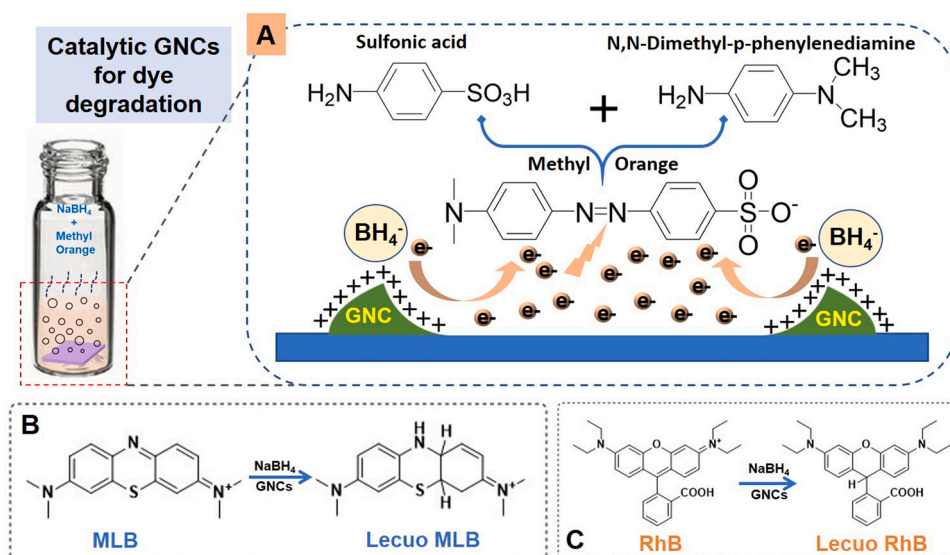
Fig. 7. (A) Mechanism of catalytic degradation of MO by GNCs, (B) and (C) Degradation reaction of RhB and MLB.

of the bounded dye molecules from the surface, resulting in the decay of the catalytic sites. Optical images of the GNCs substrate before and after 3 catalytic cycles in Figure S4 confirm the stability of catalytic substrate after the cycles.

The possible degradation mechanism of the MO dyes catalyzed by GNC substrate is illustrated in Fig. 7 A. During the process of MO degradation, $NaBH_4$ serves as an electron donor which transfers the electrons to MO. The acceptance of electrons of MO breaks its -N=N- bond, leading to the degradation to N,N-Dimethyl-p-phenylenediamine and sulfonic acid.[57] In the presence of GNC substrate, the diffusion of MO molecules and BH_4^{-1} ions to the GNC surface allows the abundance of electrons from GNC active sites to facilitate the electron transfer between the electrophilic dyes and nucleophilic BH_4^{-1} ions [50,58]. As a result, the enhancement of electron transfer to MO molecules by GNCs facilitates the rapid dye reduction. In addition, the high catalytic activity of the GNCs is also attributed to the large surface to volume ratio, high surface coverage and ordered nanostructures, all of which further improves the electron transfer efficiency thereby reducing the energy barrier during the degradation reaction. The same catalytic mechanism applies to the degradation of RhB and MLB as well with their reduction reactions shown in Fig. 7 B and C. The presence of $NaBH_4$ and GNC catalyst leads to the fast reduction of MLB and RhB to their lecuo forms [59], resulting in the decay of the dye color.

4. Conclusions

We demonstrate that sequential reactions with femtoliter droplets on a substrate can be leveraged for producing catalytic gold nanocraters in an ordered array over a large surface area. The droplets remained stable during switching the reaction solutions for ion absorption and for subsequent reduction. The final morphology of GNCs as characterized by atomic force mciroscope could be controlled by conveniently varying the duration in contact with gold precursor. The composition of GNCs was confirmed by XPS spectra. The catalytic activity of GNCs were evaluated by degradation of both anionic and cationic azo dyes in water, which could be maintained on the same level after three cycles. Our work demonstrates that sequential droplet reactions provide a new route for fabrication of surface immobilized nanomaterials. As the entire process is in a flow-in process, this novel approach offers unique flexibility in fine tuning independently the reactant concentration and reaction time in each step of the synthesis of surface-bound catalytic nanomaterials. We expect that this new approach is not limited to the

reactions for producing gold structures, but is applicable to many reactions that involve reactants in two immiscible phases. The high number of potential advantages of droplet reactions can be broadly explored in future for synthesis of other surface-bound nanomaterials.

CRediT authorship contribution statement

Xuehua Zhang: Conceptualization, Supervision. **Tulsi Satyavir Dabodiya, Haitao Yu, Miaosi Li**: Data collection. **Tulsi Satyavir Dabodiya, Haitao Yu, Miaosi Li, Xuehua Zhang**: Formal analysis. **Tulsi Satyavir Dabodiya, Miaosi Li, Xuehua Zhang**: Roles/Writing.

Declaration of Competing Interest

The authors declare that they have no known competing financial interests or personal relationships that could have appeared to influence the work reported in this paper.

Acknowledgments

Appendix A. Supporting information

Supplementary data associated with this article can be found in the online version at doi:10.1016/j.colsurfa.2022.129325.

References

[1] W. Feng, E. Ueda, P.A. Levkin, Droplet microarrays: from surface patterning to high-throughput applications, Adv. Mater. 30 (2018), 1706111.

[2] A. Raza, A.S. Alketbi, R. Devarapalli, H. Li, T. Zhang, Refractory ultrathin nanocomposite solar absorber with superior spectral selectivity and thermal stability, Adv. Opt. Mater. 8 (2020), 2000679.

[3] A. Ma, J. Xu, X. Zhang, B. Zhang, D. Wang, H. Xu, Interfacial nanodroplets guided construction of hierarchical Au, Au-Pt and Au-Pd particles as excellent catalysts, Sci. Rep. 4 (2014) 4849.

[4] B. Zheng, X. Jin, J. Liu, H. Cheng, Accelerated metal-free hydration of alkynes within milliseconds in microdroplets. ACS Sustainable, Chem. Eng. 9 (2021) 4383–4390.

[5] Z. Wei, Y. Li, R.G. Cooks, X. Yan, Accelerated reaction kinetics in microdroplets: overview and recent developments, Annu. Rev. Phys. Chem. 71 (2020) 31–51.

[6] A. Fallah-Araghi, K. Meguellati, J.-C. Baret, A. ElHarrak, T. Mangeat, M. Karplus, S. Ladame, C.M. Marques, A.D. Griffiths, Enhanced chemical synthesis at soft interfaces: A universal reaction-adsorption mechanism in microcompartments, Phys. Rev. Lett. 112 (2014), 028301.

[7] X. Han, C.S.L. Koh, H.K. Lee, W.S. Chew, X.Y. Ling, Microchemical plant in a liquid droplet: plasmonic liquid marble for sequential reactions and attomole detection of toxin at microliter scale, ACS Appl. Mater. Interfaces 9 (2017) 39635–39640.

[8] H. Yang, L. Fu, L. Wei, J. Liang, B.P. Binks, Compartmentalization of incompatible reagents within pickering emulsion droplets for one-pot cascade reactions, J. Am. Chem. Soc. 137 (2015) 1362–1371.

[9] M. Zhang, L. Wei, H. Chen, Z. Du, B.P. Binks, H. Yang, Compartmentalized droplets for continuous flow liquid-liquid interface catalysis, J. Am. Chem. Soc. 138 (2016) 10173–10183.

[10] J.K. Lee, H.S. Han, S. Chaikasetsin, D.P. Marron, R.M. Waymouth, F.B. Prinz, R. N. Zare, Condensing water vapor to droplets generates hydrogen peroxide, Proc. Natl. Acad. Sci. U. S. A 117 (2020) 30934–30941.

[11] Y. Ju, H. Zhang, W. Wang, Q. Liu, K. Yu, G. Kan, L. Liu, J. Jiang, Aqueous-microdroplet-driven abiotic synthesis of ribonucleotides. J. Phys, Chem. Lett. 13 (2022) 567–573.

[12] H. Zhang, M. Liu, F. Zhou, D. Liu, G. Liu, G. Duan, W. Cai, Y. Li, Physical deposition improved SERS stability of morphology controlled periodic micro/nanostructured arrays based on colloidal templates, Small 11 (2015) 844–853.

[13] L. Hang, F. Zhou, D. Men, H. Li, X. Li, H. Zhang, G. Liu, W. Cai, C. Li, Y. Li, Functionalized periodic Au@ MOFs nanoparticle arrays as biosensors for dual-channel detection through the complementary effect of SPR and diffraction peaks, Nano Res. 10 (2017) 2257–2270.

[14] P. García-Muñoz, F. Fresno, C. Lefevre, D. Robert, N. Keller, Ti-modified LaFeO3/β-SiC alveolar foams as immobilized dual catalysts with combined photo-fenton and photocatalytic activity, ACS Appl. Mater. Interfaces 12 (2020) 57025–57037.

[15] A. Stergiou, N. Tagmatarchis, Fluorene-perylene diimide arrays onto graphene sheets for photocatalysis, ACS Appl. Mater. Interfaces 8 (2016) 21576–21584.

[16] G. Fan, R. Ning, X. Li, X. Lin, B. Du, J. Luo, X. Zhang, Mussel-inspired immobilization of photocatalysts with synergistic photocatalytic-photothermal performance for water remediation, ACS Appl. Mater. Interfaces (2021).

[17] Y. Wang, X. Wu, B. Shao, X. Yang, G. Owens, H. Xu, Boosting solar steam generation by structure enhanced energy management, Sci. Bull. 65 (2020) 1380–1388.

[18] Y. Lu, D. Fan, H. Xu, H. Min, C. Lu, Z. Lin, X. Yang, Implementing hybrid energy harvesting in 3D spherical evaporator for solar steam generation and synergic water purification, Sol. RRL 4 (2020), 2000232.

[19] R. Li, Y. Shi, M. Wu, S. Hong, P. Wang, Photovoltaic panel cooling by atmospheric water sorption-evaporation cycle, Nat. Sustain. 3 (2020) 636–643.

[20] Q.-L. Zhu, Q. Xu, Immobilization of ultrafine metal nanoparticles to high-surface-area materials and their catalytic applications, Chem 1 (2016) 220–245.

[21] S. Moon, Q. Zhang, D. Huang, S. Senapati, H.-C. Chang, E. Lee, T. Luo, Biocompatible direct deposition of functionalized nanoparticles using shrinking surface plasmonic bubble, Adv. Mater. Interfaces 7 (2020), 2000597.

[22] G.-H. Park, K. Nielsch, A. Thomas, 2D transition metal dichalcogenide thin films obtained by chemical gas phase deposition techniques, Adv. Mater. Interfaces 6 (2019), 1800688.

[23] C. Merckle, J. Blümel, Improved rhodium hydrogenation catalysts immobilized on oxidic supports, Adv. Synth. Catal. 345 (2003) 584–588.

[24] V. Patsula, L. Kosinová, M. Lovrić, L. Ferhatovic Hamzić, M. Rabyk, R. Konefal, A. Paruzel, M. Šlouf, V. Herynek, S. Gajović, Superparamagnetic Fe3O4 nanoparticles: synthesis by thermal decomposition of iron (III) glucuronate and application in magnetic resonance imaging, ACS Appl. Mater. Interfaces 8 (2016) 7238–7247.

[25] X. Zhang, Z. Lu, H. Tan, L. Bao, Y. He, C. Sun, D. Lohse, Formation of surface nanodroplets under controlled flow conditions, Proc. Natl. Acad. Sci. U. S. A 112 (2015) 9253–9257.

[26] J. Qian, G.F. Arends, X. Zhang, Surface nanodroplets: formation, dissolution, and applications, Langmuir 35 (2019) 12583–12596.

[27] F. Gregson, J. Robinson, R. Miles, C. Royall, J. Reid, Drying kinetics of salt solution droplets: Water evaporation rates and crystallization, J. Phys. Chem. B 123 (2018) 266–276.

[28] M. Li, L. Bao, H. Yu, X. Zhang, Formation of multicomponent surface nanodroplets by solvent exchange, J. Phys. Chem. C. 122 (2018) 8647–8654.

[29] Z. Wei, M. Li, H. Zeng, X. Zhang, Integrated nanoextraction and colorimetric reactions in surface nanodroplets for combinative analysis, Anal. Chem. 92 (2020) 12442–12450.

[30] Z. Li, A. Kiyama, H. Zeng, D. Lohse, X. Zhang, Speeding up biphasic reactions with surface nanodroplets, Lab Chip 20 (2020) 2965–2974.

[31] G. Rovelli, M.I. Jacobs, M.D. Willis, R.J. Rapf, A.M. Prophet, K.R. Wilson, A critical analysis of electrospray techniques for the determination of accelerated rates and mechanisms of chemical reactions in droplets, Chem. Sci. 11 (2020) 13026–13043.

[32] R.M. Bain, C.J. Pulliam, R.G. Cooks, Accelerated Hantzsch electrospray synthesis with temporal control of reaction intermediates, Chem. Sci. 6 (2015) 397–401.

[33] D. Lohse, X. Zhang, Surface nanobubbles and nanodroplets, Rev. Mod. Phys. 87 (2015) 981.

[34] L. Bao, A.R. Rezk, L.Y. Yeo, X. Zhang, Highly ordered arrays of femtoliter surface droplets, Small 11 (2015) 4850–4855.

[35] L. Zhou, S. Yang, N. Quan, Z. Geng, S. Wang, B. Zhao, X. Wang, Y. Dong, R. Tai, J. Hu, L. Zhang, Wetting behavior of surface nanodroplets regulated by periodic nanostructured surfaces, ACS Appl. Mater. Interfaces 13 (2021) 55726–55734.

[36] Y. Xue, X. Li, H. Li, W. Zhang, Quantifying thiol-gold interactions towards the efficient strength control, Nat. Commun. 5 (2014) 1–9.

[37] I.V. Mironov, V.Y. Kharlamova, On the redox interaction of HAuCl4 with thiomalate, as well as with cysteine and glutathione in aqueous solutions, Inorg. Chim. Acta 525 (2021), 120500.

[38] M.-C. Bourg, A. Badia, R.B. Lennox, Gold- sulfur bonding in 2D and 3D self-assembled monolayers: XPS characterization, J. Phys. Chem. B. 104 (2000) 6562–6567.

[39] Y. Negishi, K. Nobusada, T. Tsukuda, Glutathione-protected gold clusters revisited: bridging the gap between gold (I)- thiolate complexes and thiolate-protected gold nanocrystals, J. Am. Chem. Soc. 127 (2005) 5261–5270.

[40] D. Men, F. Zhou, L. Hang, X. Li, G. Duan, W. Cai, Y. Li, A functional hydrogel film attached with a 2D Au nanosphere array and its ultrahigh optical diffraction intensity as a visualized sensor, C 4 (2016) 2117–2122.

[41] J. Turkevich, P.C. Stevenson, J. Hillier, A study of the nucleation and growth processes in the synthesis of colloidal gold, Faraday Discuss. 11 (1951) 55–75.

[42] M. Li, B. Dyett, H. Yu, V. Bansal, X. Zhang, Functional femtoliter droplets for ultrafast nanoextraction and supersensitive online microanalysis, Small 15 (2019), 1804683.

[43] Z. Wei, T.S. Dabodiya, J. Chen, Q. Lu, J. Qian, J. Meng, H. Zeng, H. Qian, X. Zhang, In-situ fabrication of metal oxide nanocaps based on biphasic reactions with surface nanodroplets, J. Colloid Interface Sci. 608 (2022) 2235–2245.

[44] H. Tan, S. Wooh, H.-J. Butt, X. Zhang, D. Lohse, Porous supraparticle assembly through self-lubricating evaporating colloidal ouzo drops, Nat. Commun. 10 (2019) 1–8.

[45] X. Zhang, X. Wei, W. Ducker, Formation of nanodents by deposition of nanodroplets at the polymer-liquid interface, Langmuir 26 (2010) 4776–4781.

[46] B.P. Dyett, X. Zhang, Accelerated formation of H2 nanobubbles from a surface nanodroplet reaction, ACS Nano 14 (2020) 10944–10953.

[47] G. Lin, H. Wang, W. Lu, Generation of nanodroplet reactors and their applications in in situ controllable synthesis and transportation of Ag nanoparticles, Adv. Sci. 8 (2021), 2002672.

[48] J. Piella, F. Merkoçi, A. Genç, J. Arbiol, N.G. Bastús, V. Puntes, Probing the surface reactivity of nanocrystals by the catalytic degradation of organic dyes: the effect of size, Surf. Chem. Compos. A 5 (2017) 11917–11929.

[49] K.V. Kumar, K. Porkodi, F. Rocha, Langmuir-Hinshelwood kinetics-a theoretical study, Catal. Commun. 9 (2008) 82–84.

[50] M. Sakir, M.S. Onses, Solid substrates decorated with Ag nanostructures for the catalytic degradation of methyl orange, Results Phys. 12 (2019) 1133–1141.

[51] M. Yilmaz, M. Erkartal, M. Ozdemir, U. Sen, H. Usta, G. Demirel, Three-dimensional au-coated electrosprayed nanostructured BODIPY films on aluminum foil as surface-enhanced Raman scattering platforms and their catalytic applications, ACS Appl. Mater. Interfaces 9 (2017) 18199–18206.

[52] Y. Sun, Conversion of Ag nanowires to AgCl nanowires decorated with Au nanoparticles and their photocatalytic activity, J. Phys. Chem. C. 114 (2010) 2127–2133.

[53] N.K. Mogha, S. Gosain, D.T. Masram, Gold nanoworms immobilized graphene oxide polymer brush nanohybrid for catalytic degradation studies of organic dyes, Appl. Surf. Sci. 396 (2017) 1427–1434.

[54] G.A. Khan, E.N. Esentürk, A. Bek, A.S. Bhatti, W. Ahmed, Fabrication of highly catalytically active gold nanostructures on filter-paper and their applications towards degradation of environmental pollutants, ChemistrySelect 6 (2021) 10655–10660.

[55] G. Zheng, L. Polavarapu, L.M. Liz-Marzán, I. Pastoriza-Santos, J. Pérez-Juste, Gold nanoparticle-loaded filter paper: a recyclable dip-catalyst for real-time reaction monitoring by surface enhanced Raman scattering, Catal. Commun. 51 (2015) 4572–4575.

[56] X. Fang, X. Ma, S. Xiao, M. Shen, R. Guo, X. Cao, X. Shi, Facile immobilization of gold nanoparticles into electrospun polyethyleneimine/polyvinyl alcohol nanofibers for catalytic applications, J. Mater. Chem. 21 (2011) 4493–4501.

[57] N. Garg, S. Bera, L. Rastogi, A. Ballal, M. Balaramakrishna, Synthesis and characterization of L-asparagine stabilised gold nanoparticles: Catalyst for degradation of organic dyes, Spectrochim. Acta Part A Mol. Biomol. Spectrosc. 232 (2020), 118126.

[58] M. Ismail, M. Khan, M.A. Khan, K. Akhtar, A.M. Asiri, S.B. Khan, Plant-supported silver nanoparticles: Efficient, economically viable and easily recoverable catalyst for the reduction of organic pollutants, Appl. Organomet. Chem. 33 (2019), e4971.

[59] M. Hashemi Salehi, M. Yousefi, M. Hekmati, E. Balali, Application of palladium nanoparticle-decorated Artemisia abrotanum extract-modified graphene oxide for highly active catalytic reduction of methylene blue, methyl orange and rhodamine B, Appl. Organomet. Chem. 33 (2019), e5123.